Progress In Electromagnetics Research, Vol. 125, 391–413, 2012

DESIGN AND FULL-WAVE ANALYSIS OF PIEZOELECTRIC MICRO-NEEDLE ANTENNA SENSORS FOR ENHANCED NEAR-FIELD DETECTION OF SKIN CANCER

D. Caratelli [1,*], A. Yarovoy [1], A. Massaro [2], and A. Lay-Ekuakille [3]

[1]Microwave Technology and Systems for Radar, Delft University of Technology, Mekelweg 4, 2628 CD, Delft, The Netherlands

[2]Center of Biomolecular Nanotechnology, Italian Institute of Technology, Via Morego 30, Genova 16163, Italy

[3]Department of Innovation Engineering, University of Salento, Piazza Tancredi 7, Lecce 73100, Italy

Abstract—The design and full-wave analysis of piezoelectric micro-needle antenna sensors for minimally invasive near-field detection of cancer-related anomalies of the skin is presented. To this end, an accurate locally conformal finite-difference time-domain procedure is adopted. In this way, an insightful understanding of the physical processes affecting the characteristics of the considered class of devices is achieved. This is important to improve the structure reliability, so optimizing the design cycle. In this regard, a suitable sensor layout is described, and discussed in detail. The major benefit of the proposed system stems from the potential for obtaining a superior performance in terms of input impedance matching and efficiency, in combination with an electronically tunable steering property of the near-field radiation intensity which can be profitably used to enhance the illumination and, hence, the localization of possible malignant lesions in the host medium. By using the detailed modeling approach, an extensive parametric study is carried out to analyze the effect produced on the sensor response by variations of the complex permittivity of the skin due to the presence of anomalous cells, and thus useful heuristic discrimination formulas for the evaluation of the exposure level to cancer risk are derived.

Received 12 October 2011, Accepted 9 November 2011, Scheduled 6 March 2012

* Corresponding author: Diego Caratelli (d.caratelli@tudelft.nl).

1. INTRODUCTION

Recently, considerable attention has been devoted to microwave reflectometry as an effective means for the detection and diagnosis of melanoma [1, 2]. As a matter of fact, the pre-operative discrimination between benign and cancerous tissues in the dermis and, in particular, the early prediction of potential malignancy can be carried out conveniently by measuring the electrical characteristics of the skin. In-vivo experiments have outlined that normal skin and malignant lesions differ significantly in their content of water, salts and proteins, which in turn affects the local complex permittivity value of the tissue under test [3, 4]. Thereby, the retrieval and monitoring of physiological parameters relevant to potentially harmful tumors may be achieved by evaluating the return-loss response of a suitable antenna sensor as a function of the dielectric properties at microwave frequencies of the material being investigated. Two noteworthy advantages of this approach consist in the ease of application, as well as in the absence of detrimental side effects due to the use of ionizing radiations.

In the considered context, it is pivotal to give special attention to the sensor antenna, whose design is very challenging due to the demanding requirements in terms of reduced volume occupation, low power consumption, and biocompatibility with the human body [5, 6]. Besides, the host environment consisting of different biological tissues adds substantial complexity to the problem due to the high losses [7–9]. In [1], an open-ended coaxial probe has been used to perform, in combination with a calibrated vector network analyzer (*VNA*), reflectometry-based measurements of different skin lesions in the frequency band from 300 MHz to 6 GHz. However, such a probe typically features a poor impedance matching property, which results in a large back-reflection level of the radio-frequency (*RF*) power delivered by the *VNA* oscillator and, hence, a reduced electromagnetic field interaction with the tissues under test, potentially responsible for a significant inaccuracy in the diagnosis. In order to overcome the mentioned power-budget-related limitation, a novel class of piezoelectric micro-needle antenna sensors for minimally invasive detection of skin cancer is introduced, and thoroughly investigated. The proposed devices are characterized by superior performance in terms of return loss and efficiency in the millimeter-wave frequency range. Furthermore, the adoption of a piezoelectric needle allows for an electronically controllable steering property of the near-field radiation pattern, which can be profitably used to focus the electromagnetic energy on the cancerous material [10] or, conversely, to perform a quick scan over a larger area, so providing a favorable additional degree of

freedom in the monitoring and detection procedure. A suitable layout of the proposed piezoelectric micro-sensors is in particular presented, and discussed in detail.

The complexity of the presented devices poses a non-trivial problem regarding the relevant full-wave characterization, an accurate and fast numerical scheme for solving Maxwell's equations being required. To this end, an enhanced locally conformal finite-difference time-domain ($FDTD$) technique has been used [11, 12]. The adopted electromagnetic field prediction model, featuring an enhanced numerical accuracy compared to the conventional stair-case modeling approach, is based on the definition of effective material parameters accounting for the local electrical and geometrical properties of the structure under analysis. In this way, one can gain an insight into the underlying physical processes affecting the circuital characteristics and radiation properties of the considered class of devices. This in turn is important in order to improve the sensor reliability, so optimizing the design cycle.

The paper is organized as follows. In Section 2, the layout of the proposed piezoelectric micro-needle probe sensors is detailed, whereas the full-wave $FDTD$-based modeling approach adopted for the relevant electromagnetic characterization is discussed in Section 3. A comprehensive investigation into the performance of the considered class of devices is then presented in Section 4. The concluding remarks are summarized in Section 5.

2. PROPOSED SENSOR LAYOUT

The topology of the proposed piezoelectric antenna sensor for near-field detection of cancer-related anomalies of the skin is shown in Fig. 1. As it can be readily noticed, the device features a micro-needle probe, having width $w_d = 50\,\mu\text{m}$, thickness $t_d = 12\,\mu\text{m}$, and length $l_d = 0.5\,\text{mm}$, which consists of an Aluminum Nitride (AlN) piezoelectric film sandwiched between two Molybdenum (Mo) electrodes (see Fig. 2).

The needle is assumed to be pierced through the skin in such a way as to have the circular metal shield with radius $r_g = 0.8\,\text{mm}$ and thickness $t_g = 0.25\,\text{mm}$ in close contact with the epidermis. So, once the probe is bedded in the medium being investigated, the relevant curvature radius can be adjusted electronically by applying a suitable low-frequency control voltage V_c to the Mo electrodes, with a minimally invasive impact on the surrounding biological tissues. In the proposed design layout, Molybdenum has been selected for sensor prototyping due to the low resistivity and effectiveness in promoting

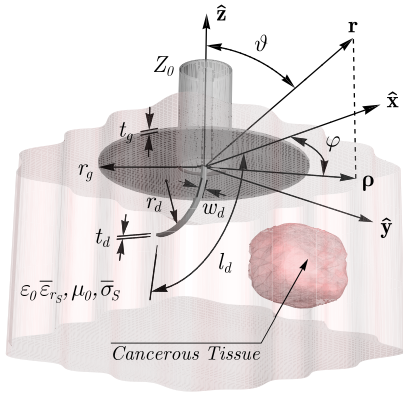

Figure 1. Geometry of the proposed micro-needle probe sensor for near-field detection of cancer-related anomalies of the skin. Structure characteristics: $l_d = 0.5\,\text{mm}$, $w_d = 50\,\mu\text{m}$, $t_d = 12\,\mu\text{m}$, $r_d = 0.4\,\text{mm}$, $r_g = 0.8\,\text{mm}$, $t_g = 0.25\,\text{mm}$. The sensor is excited by means of a coaxial feeding line having characteristic impedance $Z_0 = 50\,\Omega$. The reference system adopted to express the electromagnetic field quantities is also shown.

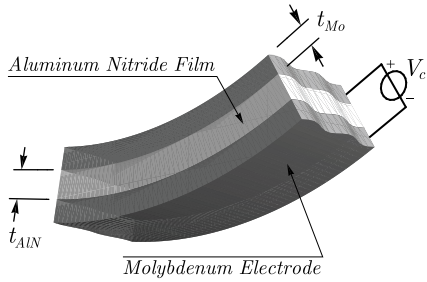

Figure 2. Geometry of the piezoelectric needle. An AlN thin film sandwiched between two Mo electrodes is used to adjust the curvature radius of the probe by applying a suitable low-frequency control voltage V_c.

a preferential orientation of the AlN film. In particular, the layers forming the sensor needle have been grown by reactive magnetron sputter technique employing a pulsed power supply [13]. The growth conditions have been optimized in order to achieve a reasonable trade-off between adhesion stability, crystallographic quality, and residual stress of the films. In this way, probes with different width values and length ranging from 250 µm to 2.5 mm have been manufactured at the

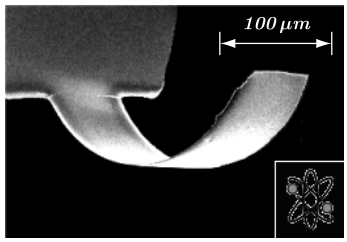

Figure 3. Scanning-electron-microscope image of a free-standing micro-needle probe prototype manufactured at the facility of the Center of Biomolecular Nanotechnology, Italian Institute of Technology, by using optical lithography and a high-precision etching technique. The piezoelectric AlN film features a thickness of 500 nm.

facility of the Center of Biomolecular Nanotechnology, Italian Institute of Technology (*IIT*), by using optical lithography and a high-precision etching technique (see Fig. 3).

The developed sensor is excited by means of a coaxial feeding line turning, at the end section, into the probing structure. The geometrical characteristics of the connector have been selected in such a way as to achieve the characteristic impedance $Z_0 = 50\,\Omega$, and a TE_{01} cut-off frequency $f_c \gg f_{\max}$, $f_{\max}$ denoting the maximum operating frequency. The outer conductor of the coaxial cable is physically connected to the metal shield, which is used to enhance the near-field radiation level at the broadside [14], while minimizing parasitic energy emission in the back direction or, conversely, reducing possible electromagnetic-interference-related problems due to the interaction with other electronic devices operating in the same environment, which potentially may result in a degradation of the device performance and, hence, an inaccurate detection and diagnosis.

3. FULL-WAVE SENSOR MODELING

The design and full-wave analysis of complex devices require accurate electromagnetic field prediction models [11, 12]. One such widely used technique is the *FDTD* technique. However, in the conventional formulation of the algorithm [15], each cell in the computational grid is implicitly assumed to be filled in by a homogeneous material. For this reason, the adoption of Cartesian meshes could result in reduced numerical accuracy where structures having complex geometry are to be modeled. In this context, the hereafter detailed locally conformal *FDTD* scheme provides a clear advantage over the use

of the stair-casing approach or unstructured and stretched space lattices, potentially suffering from significant numerical dispersion and/or instability [15]. Such scheme is based on the definition of suitable effective material tensors accounting for the local electrical and geometrical properties of the device under analysis.

Let us consider a three-dimensional domain $\mathcal{D}$ filled by a linear, isotropic, non-dispersive material, having permittivity $\varepsilon(\mathbf{r})$, magnetic permeability $\mu(\mathbf{r})$, and electrical conductivity $\sigma(\mathbf{r})$. In such a domain, a dual-space, non-uniform lattice formed by a primary and secondary Cartesian mesh is introduced. The primary mesh $\mathcal{M}_{\mathcal{D}}$ is composed of space-filling hexahedrons having nodes $\mathbf{r}_{i,j,k}$. Thereby, upon denoting the triplet $(i,j,k) \in \mathbb{N}_0^3$ as $\boldsymbol{\Upsilon}$ for shortness, the edge lengths between adjacent vertices in $\mathcal{M}_{\mathcal{D}}$ turn to be $\Delta\xi_{\boldsymbol{\Upsilon}} = \hat{\boldsymbol{\xi}} \cdot \left(\mathbf{r}_{\boldsymbol{\Upsilon}+\boldsymbol{\Lambda}_\xi} - \mathbf{r}_{\boldsymbol{\Upsilon}}\right)$, where $\boldsymbol{\Lambda}_\xi$ and $\hat{\boldsymbol{\xi}}$ are the fundamental triplet and the unit vector respectively, relevant to the ξ coordinate axis ($\xi = x, y, z$). On the other hand, the secondary or dual mesh $\widetilde{\mathcal{M}}_{\mathcal{D}}$ (see Fig. 4) consists of closed hexahedrons whose edges penetrate the shared faces of the primary cells and connect the relevant centroids $\widetilde{\mathbf{r}}_{\boldsymbol{\Upsilon}}$. As a consequence, the dual edge lengths are found to be $\ell_{\xi_{\boldsymbol{\Upsilon}}} = \hat{\boldsymbol{\xi}} \cdot \left(\widetilde{\mathbf{r}}_{\boldsymbol{\Upsilon}} - \widetilde{\mathbf{r}}_{\boldsymbol{\Upsilon}-\boldsymbol{\Lambda}_\xi}\right) = \left(\Delta\xi_{\boldsymbol{\Upsilon}-\boldsymbol{\Lambda}_\xi} + \Delta\xi_{\boldsymbol{\Upsilon}}\right)/2$. As usual, the electric field components are defined along each edge of a primary lattice cell, whereas the magnetic field components are assumed to be sampled at midpoints of the edges of the secondary lattice cells. The governing relationship between the E- and H-field components is given by Maxwell's equations in integral form, namely the Faraday-Neumann's and Ampere's laws. In particular, the enforcement of the

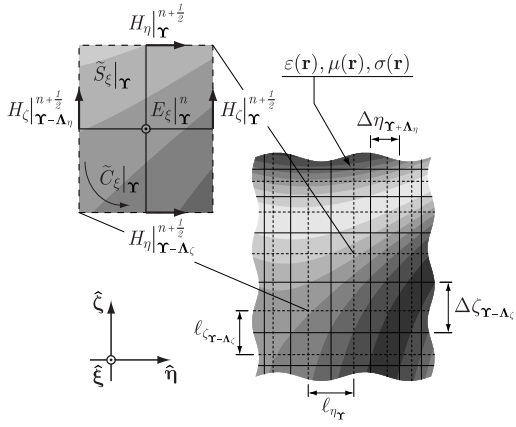

Figure 4. Cross-sectional view of the $FDTD$ computational grid in presence of a non-conformal inhomogeneous structure.

Ampere's law on the general dual-mesh cell face $\widetilde{S}_{\xi_{\boldsymbol{\Upsilon}}}$, having boundary $\partial\widetilde{S}_{\xi_{\boldsymbol{\Upsilon}}} = \widetilde{C}_{\xi_{\boldsymbol{\Upsilon}}}$ (see Fig. 4), results in the integral equation:

$$\oint_{\widetilde{C}_{\xi_{\boldsymbol{\Upsilon}}}} \mathbf{H}(\mathbf{r},t)\cdot d\boldsymbol{\ell} = \iint_{\widetilde{S}_{\xi_{\boldsymbol{\Upsilon}}}} \sigma(\mathbf{r})\, E_\xi(\mathbf{r},t)\, dS + \frac{\partial}{\partial t}\iint_{\widetilde{S}_{\xi_{\boldsymbol{\Upsilon}}}} \varepsilon(\mathbf{r})\, E_\xi(\mathbf{r},t)\, dS. \quad (1)$$

Under the assumption that the spatial increments $\Delta\xi_{\boldsymbol{\Upsilon}}$ ($\xi = x, y, z$) of the computational grid are small compared to the minimum operating wavelength, the contour integral appearing on the left-hand side of (1) can be evaluated by the mean value theorem, neglecting infinitesimal terms of higher order. Besides, the partial derivative operator in (1) can be approximated by using a central-difference approximation, which is second order-accurate where the E- and H-field components are staggered in the time domain. Therefore, upon introducing the normalized field quantities:

$$\mathcal{E}_\xi|_{\boldsymbol{\Upsilon}}^{n} = \Delta\xi_{\boldsymbol{\Upsilon}}\, E_\xi\left(\mathbf{r}_{\boldsymbol{\Upsilon}} + \frac{1}{2}\hat{\boldsymbol{\xi}}\Delta\xi_{\boldsymbol{\Upsilon}}, t_n\right), \quad (2)$$

$$\mathcal{H}_\xi|_{\boldsymbol{\Upsilon}}^{n+\frac{1}{2}} = \ell_{\xi_{\boldsymbol{\Upsilon}}}\, H_\xi\left(\widetilde{\mathbf{r}}_{\boldsymbol{\Upsilon}} - \frac{1}{2}\hat{\boldsymbol{\xi}}\Delta\xi_{\boldsymbol{\Upsilon}}, t_{n+\frac{1}{2}}\right), \quad (3)$$

with $t_\nu = \nu\Delta t$, Δt being the time step selected according to the Courant-Friedrichs-Lewy (CFL) stability condition [15], after some algebraic manipulation the following explicit time-stepping equation is obtained:

$$\mathcal{E}_\xi|_{\boldsymbol{\Upsilon}}^{n+1} = \frac{\overline{\varepsilon}_\xi|_{\boldsymbol{\Upsilon}} - \frac{1}{2}\,\overline{\sigma}_\xi|_{\boldsymbol{\Upsilon}}\,\Delta t}{\overline{\varepsilon}_\xi|_{\boldsymbol{\Upsilon}} + \frac{1}{2}\,\overline{\sigma}_\xi|_{\boldsymbol{\Upsilon}}\,\Delta t}\,\mathcal{E}_\xi|_{\boldsymbol{\Upsilon}}^{n} + \frac{\Delta t}{\overline{\varepsilon}_\xi|_{\boldsymbol{\Upsilon}} + \frac{1}{2}\,\overline{\sigma}_\xi|_{\boldsymbol{\Upsilon}}\,\Delta t}\,(\nabla\times\boldsymbol{\mathcal{H}})_\xi\Big|_{\boldsymbol{\Upsilon}}^{n+\frac{1}{2}}, \quad (4)$$

where $(\nabla\times\boldsymbol{\mathcal{H}})_\xi\Big|_{\boldsymbol{\Upsilon}}^{n+1/2} = \mathcal{H}_\zeta|_{\boldsymbol{\Upsilon}}^{n+1/2} - \mathcal{H}_\zeta|_{\boldsymbol{\Upsilon}-\boldsymbol{\Lambda}_\eta}^{n+1/2} - \mathcal{H}_\eta|_{\boldsymbol{\Upsilon}}^{n+1/2} + \mathcal{H}_\eta|_{\boldsymbol{\Upsilon}-\boldsymbol{\Lambda}_\zeta}^{n+1/2}$ denotes the finite-difference expression of the ξ-component of the normalized magnetic field curl. By applying the duality principle in the discrete space $(\mathcal{M}_\mathcal{D}, \widetilde{\mathcal{M}}_\mathcal{D})$, the $FDTD$-update equations of the H-field can be easily derived as:

$$\mathcal{H}_\xi|_{\boldsymbol{\Upsilon}}^{n+\frac{1}{2}} = \mathcal{H}_\xi|_{\boldsymbol{\Upsilon}}^{n-\frac{1}{2}} - \frac{\Delta t}{\overline{\mu}_\xi\big|_{\boldsymbol{\Upsilon}}}\,(\nabla\times\boldsymbol{\mathcal{E}})_\xi\Big|_{\boldsymbol{\Upsilon}}^{n}, \quad (5)$$

with $S_{\xi_{\boldsymbol{\Upsilon}}}$ being the general primary-mesh cell face orthogonal to the ξ coordinate axis. In (4)–(5), the information regarding the local physical properties, as well as the geometrical non-conformability of the electromagnetic structure under analysis to the adopted Cartesian mesh, is transferred to the following position-dependent effective permittivity, electrical conductivity, and permeability tensors:

$$\left\{\begin{matrix}\overline{\varepsilon}\\ \overline{\sigma}\end{matrix}\right\}_\xi\Bigg|_{\boldsymbol{\Upsilon}} = \frac{1}{\Delta\xi_{\boldsymbol{\Upsilon}}}\iint_{\widetilde{S}_{\xi_{\boldsymbol{\Upsilon}}}}\left\{\begin{matrix}\varepsilon\\ \sigma\end{matrix}\right\}(\mathbf{r})\, dS\,, \quad (6)$$

$$\overline{\mu}_{\xi}\big|_{\boldsymbol{\Upsilon}} = \frac{1}{\ell_{\xi_{\boldsymbol{\Upsilon}}}} \iint_{S_{\xi_{\boldsymbol{\Upsilon}}}} \mu(\mathbf{r})\, dS. \tag{7}$$

In this way, a significant enhancement in terms of numerical accuracy can be achieved over the conventional stair-case modeling approach. It is worth noting that the computation of the effective material parameters (6)–(7) can be conveniently carried out before the *FDTD*-method time marching starts. As a consequence, unlike in conformal techniques based on stretched computational grids, no additional correction is required in the core of the numerical algorithm.

By using the detailed sub-cell method, the design and accurate full-wave analysis of the considered class of piezoelectric micro-needle antenna sensors have been carried out. In doing so, the individual device has been meshed on a graded space lattice with maximum spatial increment $\Delta\xi_{\max} = \lambda_{\min}/20$, where $\lambda_{\min}$ denotes the wavelength in the skin at the maximum operating frequency in the spectrum of the excitation signal, which is a Gaussian-modulated sinusoidal voltage pulse defined by:

$$\Pi_g(t) = \exp\left[-\left(\frac{t-t_0}{T_g}\right)^2\right] \sin(2\pi f_c t)\, u(t)\,, \tag{8}$$

where $u(t)$ is the usual unit-step distribution, and:

$$\frac{t_0}{4} = T_g = \frac{2\sqrt{\ln 10}}{\pi B}. \tag{9}$$

The selection of the time parameter T_g according to (9) results in the significant spectral content of the source pulse, measured at $-10\,\mathrm{dB}$ level, within the frequency band from $f_{\min} = f_c - B/2$ to $f_{\max} = f_c + B/2$. The energy delivered by the voltage generator, assumed to feature internal resistance R_g, is accounted for by adding a local current density term in the finite-difference equations used to update the transient distribution of the electric field at the feed section of the sensor probe:

$$\mathcal{E}_{\xi}\big|_{\boldsymbol{\Upsilon}_g}^{n+1} = \frac{\overline{\varepsilon}_{\xi}\big|_{\boldsymbol{\Upsilon}_g} - \frac{\Delta t}{2R_g}}{\overline{\varepsilon}_{\xi}\big|_{\boldsymbol{\Upsilon}_g} + \frac{\Delta t}{2R_g}}\, \mathcal{E}_{\xi}\big|_{\boldsymbol{\Upsilon}_g}^{n} + \frac{\Delta t}{\overline{\varepsilon}_{\xi}\big|_{\boldsymbol{\Upsilon}_g} + \frac{\Delta t}{2R_g}} \left[(\nabla \times \boldsymbol{\mathcal{H}})_{\xi}\Big|_{\boldsymbol{\Upsilon}_g}^{n+\frac{1}{2}} + \mathcal{I}_g\big|^{n+\frac{1}{2}} \right], \tag{10}$$

$\boldsymbol{\Upsilon}_g$ being the index triplet relevant to the driving point, and where $\mathcal{I}_g\big|^{n+1/2} = \Pi_g\big(t_{n+1/2}\big)/R_g$ denotes the discrete-valued excitation current. In this way, the voltage and current accepted at the input terminals of the feeding line can be computed as follows:

$$v_{in}(t_n) = -\int_{C_V} \mathbf{E}(\mathbf{r}, t_n) \cdot d\boldsymbol{\ell} \simeq -\,\mathcal{E}_{\xi}\big|_{\boldsymbol{\Upsilon}_g}^{n}\,, \tag{11}$$

$$i_{in}\left(t_{n+\frac{1}{2}}\right) = \oint_{C_I} \mathbf{H}\left(\mathbf{r}, t_{n+\frac{1}{2}}\right) \cdot d\boldsymbol{\ell} \simeq \left(\nabla \times \boldsymbol{\mathcal{H}}\right)_{\xi}\Big|_{\boldsymbol{\Upsilon}_g}^{n+\frac{1}{2}}, \tag{12}$$

where C_V is an open contour extending along the driving point, and C_I a closed contour path wrapping around the generator. Thereupon, the input impedance of the device is readily evaluated as:

$$Z_{in}(f) = e^{j\pi f \Delta t} \frac{\mathcal{DFT}\{v_{in}(t_n)\}(f)}{\mathcal{DFT}\left\{i_{in}\left(t_{n+\frac{1}{2}}\right)\right\}(f)}, \tag{13}$$

with $\mathcal{DFT}\{\cdot\}(f)$ being the usual discrete Fourier transform operator, and where the correction term $e^{j\pi f \Delta t}$ accounts for the half-time-step staggering inherent in the *FDTD*-method marching algorithm.

In all numerical simulations carried out within the proposed research, a ten-cell uniaxial-perfectly-matched-layer (*UPML*) absorbing boundary condition [16] has been adopted to simulate the extension of the space lattice to infinity. In particular, a quartic polynomial grading of the *UPML* conductivity profile has been selected in such a way as to achieve a nominal value $\mathcal{R}_{PML} \simeq 10^{-4}$ of the spurious reflection level at the truncation of the computational mesh. As outlined in [15], the *UPML* is indeed perfectly matched to inhomogeneous material regions, as the one formed by the skin layer being investigated during the sensing survey and the upper air region, so no spurious numerical reflection takes place at the termination of the air-skin interface. However, in order to avoid the numerical instability of the time-stepping scheme within *UPML* due to the dispersive behavior of the skin, a suitable frequency-domain averaging approach has been adopted. As a matter of fact, the skin layer is modeled as a half space having effective relative dielectric constant $\overline{\varepsilon}_{r_S}$ and electrical conductivity $\overline{\sigma}_S$ computed, by means of the integral mean value theorem, as:

$$\overline{\varepsilon}_{r_S} = \frac{1}{B}\int_{f_{\min}}^{f_{\max}} \mathrm{Re}\left\{\varepsilon^*_{r_S}(f)\right\} df\,, \tag{14}$$

$$\overline{\sigma}_S = -\frac{1}{B}\int_{f_{\min}}^{f_{\max}} 2\pi f \varepsilon_0 \mathrm{Im}\left\{\varepsilon^*_{r_S}(f)\right\} df, \tag{15}$$

respectively, ε_0 denoting the free-space permittivity and $\varepsilon^*_{r_S}(f)$ the complex relative dielectric constant described by the following experimentally extrapolated Cole-Cole-like fitting equation [17]:

$$\varepsilon^*_{r_S}(f) = \varepsilon_{r_\infty} + \frac{\Delta\varepsilon_r}{1 + (j2\pi f\tau)^{1-\alpha}} + \frac{\sigma_i}{j2\pi f \varepsilon_0}\,, \tag{16}$$

where ε_{r_∞} is the optical relative permittivity, τ the relaxation time, $\Delta\varepsilon_r$ the magnitude of the dispersion of free water fraction in the

Table 1. Parameters of the cole-cole-like dispersion model relevant to the skin of the wrist/forearm [17].

ε_{r_∞}	τ (ps)	$\Delta\varepsilon_r$	σ_i (S/m)	α
8.35	7.13	20.5	0.5	0.064

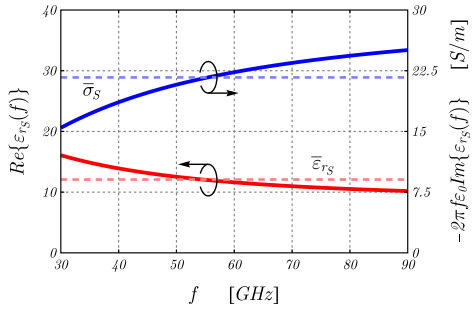

Figure 5. Frequency-domain behavior of the complex permittivity relevant to the skin of the wrist/forearm [17]. The integral mean values of the relative dielectric constant and electrical conductivity in the range from $f_{\min} = 30\,\text{GHz}$ to $f_{\max} = 90\,\text{GHz}$ are also shown.

skin layer, σ_i the ionic conductivity, and α characterizes the spread in relaxation time. These model parameters strongly depends on the part of the body being analyzed, the ones relevant to the wrist/forearm being listed in Table 1 for convenience of the reader [17].

4. SENSOR RADIATION PROPERTIES AND CIRCUITAL CHARACTERISTICS

By using the detailed locally conformal *FDTD* technique, the circuital characteristics and radiation properties of the proposed class of sensing devices have been investigated in detail in the frequency range from $f_{\min} = 30\,\text{GHz}$ to $f_{\max} = 90\,\text{GHz}$ ($f_c = B = 60\,\text{GHz}$) where, according to Equations (14)–(16) and the experimental physiological parameters listed in Table 1, the skin of the wrist/forearm exhibits an integral average relative permittivity $\overline{\varepsilon}_{r_S} \simeq 12.08$ and electrical conductivity $\overline{\sigma}_S \simeq 21.67\,\text{S/m}$ (see Fig. 5).

A specific parametric analysis has been carried out in order to determine the impact of the curvature radius r_d of the micro-needle probe on the sensor performance in terms of impedance matching, as well as with regard to the total efficiency $e_a(f)$, given by:

$$e_a(f) = e_{in}(f)\, e_r(f)\,, \tag{17}$$

where:

$$e_r(f) = \frac{P_{rad}(f)}{P_{in}(f)}, \tag{18}$$

$$e_{in}(f) = 1 - |\Gamma_{in}(f)|^2, \tag{19}$$

denote the radiation and mismatch efficiency terms respectively, $\Gamma_{in}(f) = [Z_{in}(f) - Z_0]/[Z_{in}(f) + Z_0]$ being the input reflection coefficient. In (18), $P_{in}(f) = \frac{1}{2}\mathrm{Re}\{V_{in}(f)\, I^*_{in}(f)\}$ is the real input power accepted by the sensor bedded in the tissue under test, whereas the total radiated power $P_{rad}(f)$ is determined by integrating the real part of the Poynting vector over a surface S_a enclosing the device, namely:

$$P_{rad}(f) = \frac{1}{2}\mathrm{Re}\left\{\iint_{S_a} \mathbf{E}(\mathbf{r}, f) \times \mathbf{H}(\mathbf{r}, f)^* \cdot d\mathbf{S}\right\}. \tag{20}$$

As it can be noticed in Fig. 6, the sensor is well matched to the feeding line in a ultra-wide band starting from the lower cut-off frequency at 10 dB return-loss level $\nu_{\min} \simeq 44.25$ GHz, which is not severely impacted by the curvature radius of the probe. On the other hand, the reactive energy storage process occurring in the spatial region between the needle and the metal shield results in a capacitive effect which significantly affects the upper cut-off frequency $\nu_{\max}$ and, hence, the operating bandwidth $BW = \nu_{\max} - \nu_{\min}$, whose behavior as a

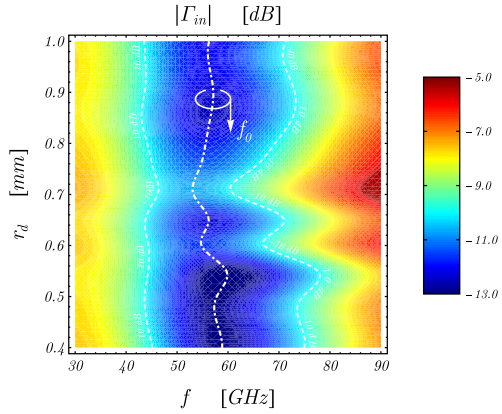

Figure 6. Frequency-domain behavior of the input reflection coefficient featured by the micro-needle sensor as a function of the curvature radius r_d of the probe. The fundamental resonant frequency f_0 of the device is also shown. Structure characteristics: $l_d = 0.5$ mm, $w_d = 50$ µm, $t_d = 12$ µm, $r_g = 0.8$ mm, $t_g = 0.25$ mm.

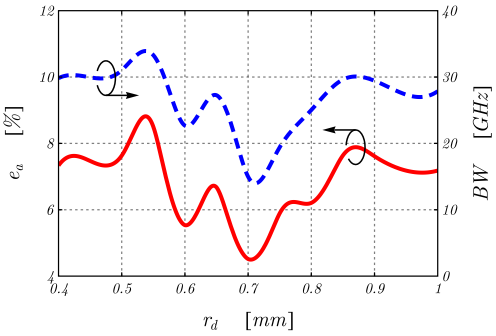

Figure 7. Operating bandwidth BW at 10 dB return-loss level and total efficiency e_a at the central working frequency f_c as functions of the curvature radius r_d of the sensor probe. Structure characteristics: $l_d = 0.5\,\text{mm}$, $w_d = 50\,\mu\text{m}$, $t_d = 12\,\mu\text{m}$, $r_g = 0.8\,\text{mm}$, $t_g = 0.25\,\text{mm}$.

function of r_d is shown in Fig. 7. It has been numerically found out that the considered sensor features a nearly flat fractional bandwidth $FBW = BW/f_0$, f_0 being the fundamental resonant frequency (see Fig. 6), whereas the related radiation quality factor [18] is given by:

$$Q \simeq \frac{s-1}{\sqrt{s}} \frac{1}{FBW} \simeq 4\,Q_C, \tag{21}$$

with $Q_C = 1/\left(\overline{k}_S r_g\right) + 1/\left(\overline{k}_S r_g\right)^3$ denoting the Chu lower bound [19] at the fundamental wave number $\overline{k}_S = 2\pi f_0 \sqrt{\overline{\varepsilon}_{r_S}}/c_0$ in the skin layer. In (21), $s \simeq 2$ is the level of the voltage-standing-wave-ratio ($VSWR$) at which FBW is determined. Inspection of Fig. 7 also reveals that the total efficiency e_a of the sensor at the central working frequency f_c assumes reasonably high values ($\gtrsim 4.5\%$) despite of the high losses of the host medium. In this respect, it is to be stressed out that e_a is strongly correlated to BW; as a matter of fact, the following equation can be derived heuristically:

$$e_a \simeq BW/4\,, \tag{22}$$

showing that the level of power deployed in the skin increases as the operating bandwidth becomes larger. In (22), BW is assumed to be expressed in GHz, and e_a in percentage (%). Therefore, the input impedance matching of the device under analysis is an important functional characteristic which is to be properly taken into account during the design stage.

The major benefit of the proposed system stems from the potential for controlling the relevant radiation properties by means of the piezoelectric micro-needle probe. Fig. 8 clearly illustrates some key

effects of the curvature radius in this regard; shown is the near-field pattern evaluated along the E-plane of the structure at a depth $d_s = 1.3\,\text{mm}$ in the unaltered medium with nominal complex permittivity. As it appears from Fig. 8, reducing r_d is an effective means to achieve a quasi-uniform distribution of the field intensity over a wider region around the broadside direction. That is in turn important to enhance the illumination and, thereby, the localization of possible malignant tissues. To this end, the selection of the curvature radius value $r_d = 0.4\,\text{mm}$ provides a good compromise between near-field radiation properties and efficiency (see Fig. 7), while keeping good performance in terms of reduced reflection coefficient at the input terminals of the device.

In order to gain a physical insight into the emission characteristics featured by the proposed sensor, the transient behavior of the electric field radiated by the structure in the skin has been investigated at the time instants $\tau_s^{\mp} = t_0 \mp T_g$ [see Equation (9)]. In this way, it has been pointed out that the good coverage at the boresight is substantially due to the energy leakage of the current wave flowing along the curved probing needle. This specific process leads to the excitation of a number of successive wavefronts W_{v_i} $(i = 1, 2, \ldots)$, which are to a good approximation circles centered at the virtual phase center having Cartesian coordinates $x = -r_d$, $y = z = 0$ (see Fig. 9). As a consequence, it is straightforward to infer that, in the general space point within the host medium, the time of arrival of the radio signal relevant to the first-order wavefront W_{v_1} changes with the

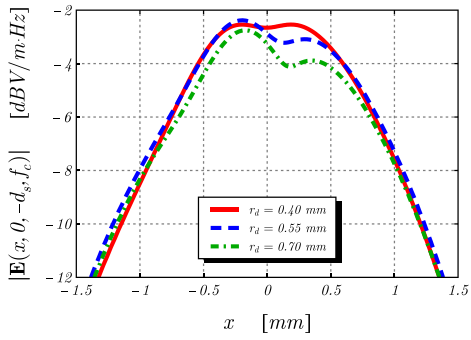

Figure 8. Near-field pattern along the E-plane ($y = 0$) of the sensor at a depth $d_s = 1.3\,\text{mm}$ in the unaltered skin with nominal complex permittivity for different curvature radii of the probe. Structure characteristics: $l_d = 0.5\,\text{mm}$, $w_d = 50\,\mu\text{m}$, $t_d = 12\,\mu\text{m}$, $r_g = 0.8\,\text{mm}$, $t_g = 0.25\,\text{mm}$. Operating frequency: $f_c = 60\,\text{GHz}$.

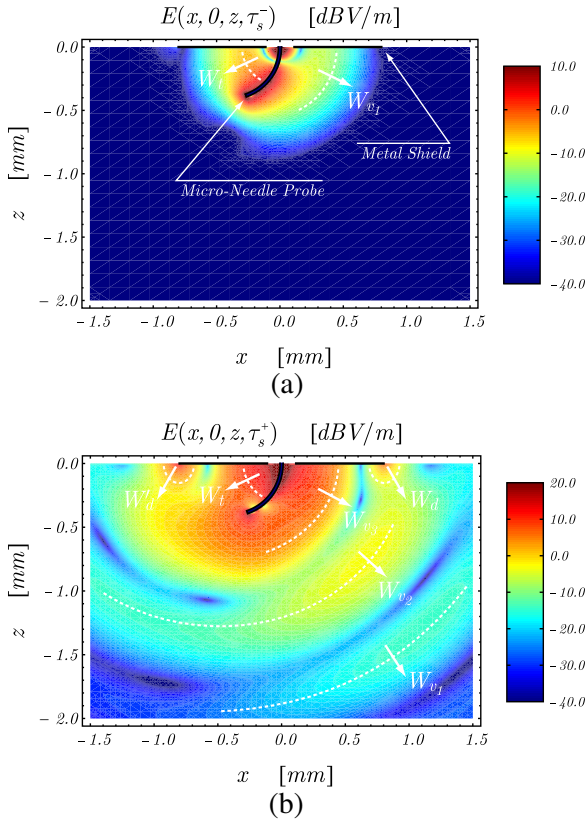

Figure 9. Magnitude of the electric field excited along the E-plane ($y = 0$) of the sensor at the time instant (a) $\tau_s^- = t_0 - T_g$ and (b) $\tau_s^+ = t_0 + T_g$. The wavefronts relevant to the energy leakage of the current wave flowing along the needle probe, as well as the diffraction processes occurring at the truncation of the ground plane can be noticed. Structure characteristics: $l_d = 0.5\,\text{mm}$, $w_d = 50\,\mu\text{m}$, $t_d = 12\,\mu\text{m}$, $r_g = 0.8\,\text{mm}$, $t_g = 0.25\,\text{mm}$.

elevation angle of observation ϑ as:

$$\tau_{v_1} \simeq t_0 + \frac{\sqrt{r^2 + r_d^2 + 2rr_d\cos\vartheta}}{c_0}\sqrt{\bar{\varepsilon}_{r_S}}\ . \tag{23}$$

Besides, it is worth noting that the peculiar geometrical configuration of the sensor results in an additional travelling-wave-like radiation process, with wavefront W_t, originating in the tapered spatial region, between the probe and the metal shield, which may be actually

regarded as a vee-monopole structure [20]. Thanks to that, no deep nulls are observed in the near-field intensity distribution. As it can be noticed in Fig. 9(b), the interaction of the radio-wave contributions from the feed section with the truncation of the shielding disk is responsible for the excitation of two diffraction wavefronts W_d and W'_d. The diffracted field propagates back to the driving point generating secondary emission/diffraction phenomena. The process then repeats and results in the well-known ringing effect [21], which should be properly taken into account during the prototyping stage of the design to optimize the sensor performance. To this end, a rolled termination of the shield might be used, in addition to a suitable absorber, to minimize edge diffraction and, thereby, produce a well controlled radiation pattern. It is, anyhow, to be pointed out that the lossy characteristics of the dermis already play a significant role to mitigate the level of the mentioned parasitic reflections, as well as undesired fluctuations in the input impedance.

In order to further analyze the characteristics of the electromagnetic field transmitted in the skin, the footprint of the proposed device at the depth $d_s = 1.3\,\text{mm}$ in the unaltered medium with nominal material parameters has been evaluated at the central working frequency f_c. The footprint, representing the effective area illuminated by the sensor on the skin surface or subsurface, provides important information in the radio-frequency monitoring of cancer-related anomalies. As a matter of fact, a small or defocused footprint makes the detection of abnormal tissues difficult because of the reduced strength of the target back-scattering response. So, an optimal footprint is of fundamental importance to enhance the assessment and diagnosis of possible health vulnerabilities. As commonly done in the realm of ground penetrating radar (*GPR*) applications [22–25], the footprint can be determined as the normalized peak-value distribution of the electric field tangential to the observation plane at depth $d \geq 0$, namely:

$$FP(x, y \mid d, f) = \frac{E_\tau(x, y, -d, f)}{\max\limits_{(x,y)\in\mathbb{R}^2} E_\tau(x, y, -d, f)}\,. \tag{24}$$

Fig. 10 demonstrates that the radius ρ_{FP} of the $-3\,\text{dB}$ subsurface footprint featured by the proposed sensor in the near-field region is closely related to the dimension of the device, namely the size r_g of the ground plane acting as a reflector. Furthermore, it has been numerically found that, for significant depths of observation in the skin, ρ_{FP} tends to reduce as r_g becomes larger. Although the computed maps are not shown here for the sake of brevity, this property can be readily inferred by considering the Fourier-transform relationship holding between a given aperture current distribution and

the relevant far-field pattern [26]. So, one can conclude that the size of the footprint can be adjusted by varying the effective aperture of the structure. This concept forms the basis for developing future-generation class of sensors with electronically tunable characteristics. As pointed out in the time domain, the radiated energy tends to be focused in an angular sector centered on the broadside direction where the curvature radius of the micro-needle probe is properly selected (see Fig. 10(a)). On the contrary, when, in the initial stage of the monitoring procedure, the needle is pierced through the skin in vertical position, the sensor footprint assumes, as expected from linear antenna theory, a donut-like shape with a deep radiation null at the boresight (see Fig. 10(b)), potentially resulting in a masking of the target and, hence, an inaccurate diagnosis.

A key role in the design of the considered sensing devices is played by the radius r_g of the metal shield. In order to provide the reader with essential information in this respect, a comprehensive investigation into the structure performance in terms of impedance matching and radiation properties has been carried out. The parametric study of the frequency-domain behavior of the input reflection coefficient has shown that the ground plane size has a strong impact on the operating bandwidth BW at 10 dB return-loss level (see Fig. 11), the maximum $BW_{\max} \simeq 32\,\text{GHz}$ being obtained for $r_g \simeq \overline{\lambda}_S/2 \simeq 0.8\,\text{mm}$ where

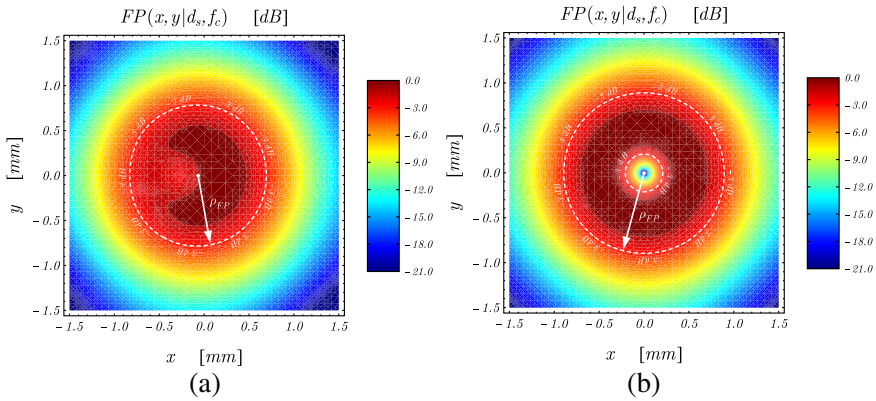

Figure 10. Subsurface footprint featured by the sensor with curvature radius $r_d = 0.4\,\text{mm}$ (a) and $r_d \to +\infty$ (b) at a depth $d_s = 1.3\,\text{mm}$ in the unaltered skin with nominal complex permittivity. Structure characteristics: $l_d = 0.5\,\text{mm}$, $w_d = 50\,\mu\text{m}$, $t_d = 12\,\mu\text{m}$, $r_g = 0.8\,\text{mm}$, $t_g = 0.25\,\text{mm}$. Operating frequency: $f_c = 60\,\text{GHz}$. The deep radiation null at the boresight for $r_d \to +\infty$ can be noticed.

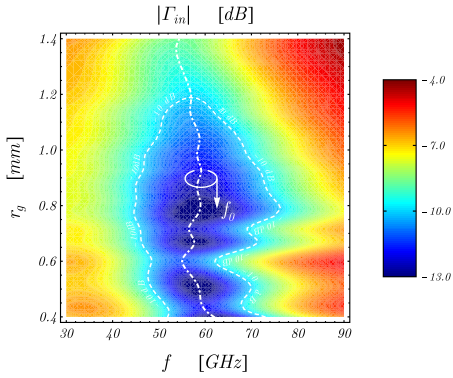

Figure 11. Frequency-domain behavior of the input reflection coefficient featured by the micro-needle sensor as a function of the radius r_g of the metal shield. The fundamental resonant frequency f_0 of the device is also shown. Structure characteristics: $l_d = 0.5\,\text{mm}$, $w_d = 50\,\mu\text{m}$, $t_d = 12\,\mu\text{m}$, $r_d = 0.4\,\text{mm}$, $t_g = 0.25\,\text{mm}$.

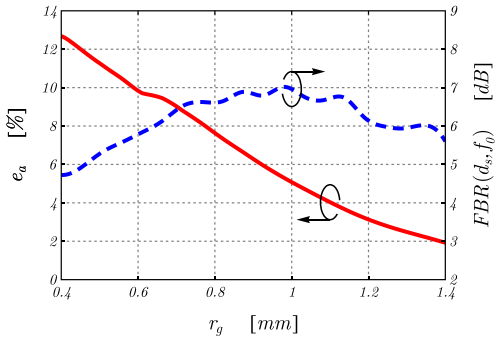

Figure 12. Near-field front-to-back radiation ratio (FBR) at the observation distance $d_s = 1.3\,\text{mm}$ and total efficiency e_a at the resonance as functions of the radius r_g of the metal shield. Structure characteristics: $l_d = 0.5\,\text{mm}$, $w_d = 50\,\mu\text{m}$, $t_d = 12\,\mu\text{m}$, $r_d = 0.4\,\text{mm}$, $t_g = 0.25\,\text{mm}$.

$\overline{\lambda}_S = 2\pi/\overline{k}_S$ denotes the fundamental wavelength in the skin layer. On the other hand, as it appears from Fig. 11, the impedance matching of the sensor to the feeding line is severely jeopardized wherein a radius $r_g \gtrsim 4\overline{\lambda}_S/5 \simeq 1.2\,\text{mm}$ is selected. Fig. 11 also demonstrates the important conclusion that the dimension of the metal shield has no significant influence on the resonant frequency f_0, unless the ground plane size is reduced below the threshold $r_g \simeq 2\overline{\lambda}_S/5 \simeq 0.6\,\text{mm}$. The

total efficiency of the structure has been computed at the resonance in order to examine the relevant radiation characteristics. In doing so, the following heuristic equation has been found to hold true with a good degree of confidence (see Fig. 12):

$$e_a \simeq 16.75 - 11.25\, r_g, \tag{25}$$

where r_g is expressed in mm, and e_a in percentage. However, it is to be stressed out that the level of power deployed in the host medium does not necessarily increase and, conversely, a substantial spurious emission may occur in the air region as r_g becomes smaller. To clarify this point, a dedicated analysis has been carried out by investigating the sensor behavior in terms of near-field front-to-back radiation ratio, defined as follows:

$$FBR(d, f) = 20 \log \frac{|\mathbf{E}(0, 0, -d, f)|}{|\mathbf{E}\,(0, 0, d, f)|}\,, \tag{26}$$

d denoting the observation depth in the dermis. As it can be inferred, such figure of merit is conveniently introduced to quantify the electromagnetic-field focusing properties of the device. In Fig. 12, one can notice that the back-radiation level is actually a non-monotone function, directly related to the metal shield radius in the range $r_g \lesssim 2\overline{\lambda}_S/3 \simeq 1.0\,\mathrm{mm}$. On the basis of the heuristically derived Equation (22), the computed results clearly reveal that the design value $r_g \simeq \overline{\lambda}_S/2$ provides a good trade-off between circuital characteristics, efficiency, and parasitic energy emission. That in turn is useful to reduce potential electromagnetic interferences (EMIs) due to the interaction with nearby electronic equipment. Furthermore, where the suggested ground plane size is adopted for the manufacturing, a superior performance in terms of quasi-uniformity of the field intensity distribution at the boresight is achieved (see Fig. 13) so enhancing the illumination of possible malignant lesions and, hence, the target detectability.

By using the specified optimal geometrical parameters, an extensive parametric study has been finally performed to analyze the effect produced on the sensor response by variations of the relative permittivity $\Delta\overline{\varepsilon}_{r_S}/\overline{\varepsilon}_{r_S}$, and electrical conductivity $\Delta\overline{\sigma}_S/\overline{\sigma}_S$ of the skin due to the presence of anomalous tissues with different content of water, salts and proteins (see Fig. 14). In this way, it has been pointed out that the relative variation on the fundamental resonant frequency f_0 of the device is closely described by the fitting equation:

$$\frac{\Delta f_0}{f_0} \simeq -0.3\frac{\Delta\overline{\varepsilon}_{r_S}}{\overline{\varepsilon}_{r_S}} + 0.025\frac{\Delta\overline{\sigma}_S}{\overline{\sigma}_S}\,, \tag{27}$$

where the involved quantities are all expressed in percentage. On the other hand, the operating bandwidth BW at 10 dB return-loss

level features a more complex behavior, and tends to reduce to zero in the parameter domain $\Delta\overline{\varepsilon}_{rS}/\overline{\varepsilon}_{rS} + \Delta\overline{\sigma}_S/\overline{\sigma}_S \gtrsim 77.5\%$, because of the large back-reflection to the feeding line. The presented data and

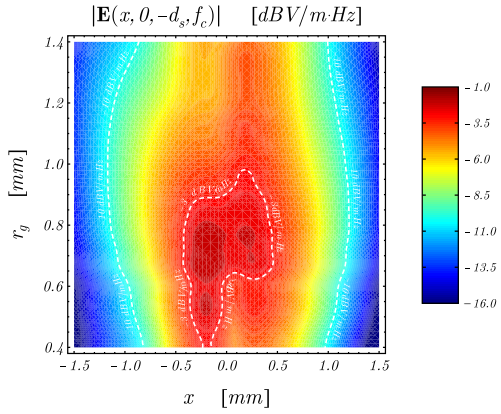

Figure 13. Near-field pattern along the E-plane ($y = 0$) of the sensor at a depth $d_s = 1.3\,\text{mm}$ in the unaltered skin with nominal complex permittivity as a function of the radius r_g of the metal shield. Structure characteristics: $l_d = 0.5\,\text{mm}$, $w_d = 50\,\mu\text{m}$, $t_d = 12\,\mu\text{m}$, $r_d = 0.4\,\text{mm}$, $t_g = 0.25\,\text{mm}$. Operating frequency: $f_c = 60\,\text{GHz}$.

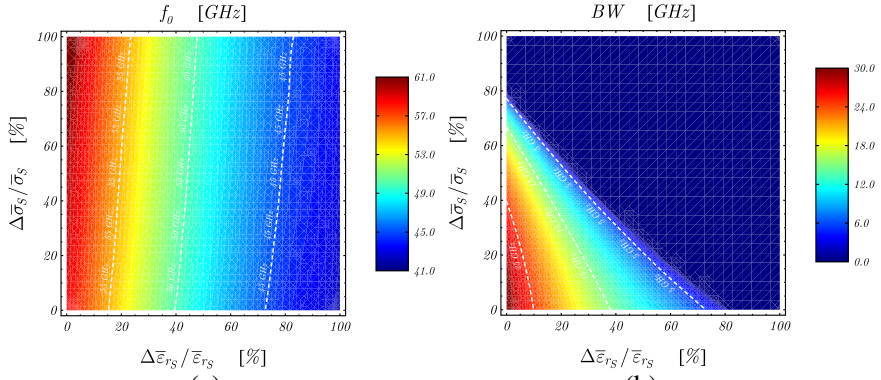

Figure 14. (a) Fundamental resonant frequency f_0 and (b) operating bandwidth BW at 10 dB return-loss level as functions of the variations of the relative permittivity $\Delta\overline{\varepsilon}_{rS}/\overline{\varepsilon}_{rS}$, and electrical conductivity $\Delta\overline{\sigma}_S/\overline{\sigma}_S$ of the skin due to the presence of potentially cancerous tissues. Structure characteristics: $l_d = 0.5\,\text{mm}$, $w_d = 50\,\mu\text{m}$, $t_d = 12\,\mu\text{m}$, $r_d = 0.4\,\text{mm}$, $r_g = 0.8\,\text{mm}$, $t_g = 0.25\,\text{mm}$.

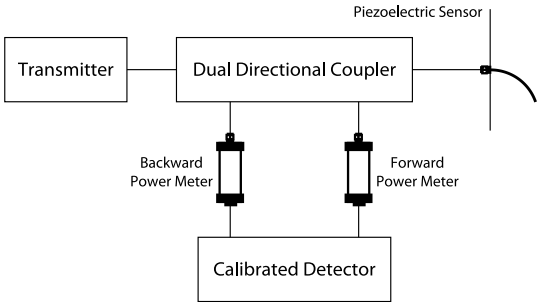

Figure 15. Experimental measurement layout for a reflectometry-based discrimination of the risk level due to the presence of cancer-related anomalies of the skin. A dual directional coupler is used, in combination with a high-sensitivity detector, to evaluate the characteristics, in terms of resonant frequency and operating bandwidth, featured by the sensor bedded in the medium under test.

design formulas provide useful information in a reflectometry-based detection procedure of the skin cancer. In this regard, it is to be noticed that the bandwidth-frequency points relevant to different risk levels can be easily discriminated by using a dual directional coupler [27] in combination with a suitable high-sensitivity receiver, as shown in Fig. 15.

5. CONCLUSION

The design and full-wave characterization of piezoelectric micro-needle antenna sensors for near-field detection of cancer-related anomalies of the skin has been presented. To this end, an accurate locally conformal *FDTD* procedure has been adopted. In this way, a detailed and insightful understanding of the physical processes affecting the circuital characteristics and radiation properties of the considered class of devices has been gained. This in turn is of crucial importance to enhance the structure reliability, so optimizing the design cycle. In this respect, an experimental sensor layout has been discussed in detail. Specifically, an AlN piezoelectric film sandwiched between Mo electrodes is used to adjust the curvature radius of the micro-needle probe by application of a suitable low-frequency control voltage, with a minimally invasive impact on the surrounding biological material.

The major benefit of the proposed system stems from the potential for achieving a superior performance in terms of input impedance matching and efficiency, in combination with an electronically tunable

steering property of the near-field radiation pattern which can be profitably used to focus the electromagnetic energy or, conversely, to get a quasi-uniform distribution of the field intensity over a wider angular sector along the broadside direction within the host medium. Such capability is essential to enhance the illumination and, hence, the detection of possible malignant lesions, so providing a favorable additional degree of freedom in the detection procedure. By using the detailed modeling approach, an extensive parametric study has been carried out to analyze the effect produced on the sensor response by variations of the relative permittivity and electrical conductivity of the skin due to the presence of anomalous cells, and thus useful heuristic discrimination formulas have been derived. In this way, one can retrieve information about the growth rate of potentially cancerous tissues, which is a very important aspect regarding the monitoring of the risk.

In future studies, an extensive analysis of the feeding section, as well as a detailed investigation of the control mechanism of the piezoelectric probe are to be presented, in view of the experimental verification and assessment of the diagnosis accuracy achievable with the proposed class of sensors in real-life clinical surveys.

ACKNOWLEDGMENT

The authors would like to acknowledge Prof. R. Cingolani, Italian Institute of Technology (*IIT*), for useful discussions on the prototyping of piezoelectric micro-needle probes, and for contributing with his constructive remarks to the improvement of the quality of this work.

REFERENCES

1. Mehta, P., K. Chand, D. Narayanswamy, D. G. Beetner, R. Zoughi, and W. V. Stoecker, "Microwave reflectometry as a novel diagnostic tool for detection of skin cancers," *IEEE Trans. Instrum. Meas.*, Vol. 55, No. 4, 1309–1316, Aug. 2006.
2. Uribe, A. G., J. M. Hong, J. Zou, and L. V. Wang, "Micromachined oblique incidence reflectometry (OIR) probe for skin cancer detection," *Proc. International Solid-State Sensors, Actuators and Microsystems Conference*, 1099–1102, Lyon, France, Jun. 10–14, 2007.
3. Suntzeff, V. and C. Carruthers, "The water content in the epidermis of mice undergoing carcinogenesis by methylcholanthrene," *Cancer Res.*, Vol. 6, 574–577, 1946.

4. Beetner, D. G., S. Kapoor, S. Manjunath, X. Zhou, and W. V. Stoecker, "Differentiation among basal cell carcinoma, benign lesions, and normal skin using electric impedance," *IEEE Trans. Biomed. Eng.*, Vol. 50, No. 8, 1020–1025, Aug. 2003.
5. Klemm, M., I. Z. Kovacs, G. F. Pedersen, and G. Troster, "Novel small-size directional antenna for UWB WBAN/WPAN applications," *IEEE Trans. Antennas Propagat.*, Vol. 53, No. 12, 3884–3896, Dec. 2005.
6. Gemio, J., J. Parron, and J. Soler, "Human body effects on implantable antennas for ism bands applications: Models comparison and propagation losses study," *Progress In Electromagnetics Research*, Vol. 110, 437–452, 2010.
7. Chatterjee, I., M. J. Hagmann, and O. P. Gandhi, "Plane-wave spectrum approach for the calculation of electromagnetic absorption under near-field exposure conditions," *Bioelectromagnetics*, Vol. 1, No. 4, 363–377, 1980.
8. Chatterjee, I., M. J. Hagmann, and O. P. Gandhi, "Electromagnetic absorption in a multilayered slab model of tissue under near-field exposure conditions," *Bioelectromagnetics*, Vol. 1, No. 4, 379–388, 1980.
9. Klemm, M. and G. Troester, "EM energy absorption in the human body tissues due to UWB antennas," *Progress In Electromagnetics Research*, Vol. 62, 261–280, 2006.
10. Iero, D., T. Isernia, A. F. Morabito, I. Catapano, and L. Crocco, "Optimal constrained field focusing for hyperthermia cancer therapy: A feasibility assessment on realistic phantoms," *Progress In Electromagnetics Research*, Vol. 102, 125–141, 2010.
11. Caratelli, D. and R. Cicchetti, "A full-wave analysis of interdigital capacitors for planar integrated circuits," *IEEE Trans. Magnetics*, Vol. 39, No. 3, 1598–1601, May 2003.
12. Caratelli, D., A. Massaro, R. Cingolani, and A. Yarovoy, "Accurate time-domain modeling of reconfigurable antenna sensors for non-invasive melanoma skin cancer detection," *IEEE Sens. J.*, 2011.
13. Dubois, M.-A. and P. Muralt, "Properties of aluminum nitride thin films for piezoelectric transducers and microwave filter applications," *Appl. Phys. Lett.*, Vol. 74, No. 20, 3032–3034, 1999.
14. Caratelli, D., R. Cicchetti, G. Bit-Babik, and A. Faraone, "Circuit model and near-field behavior of a novel patch antenna for WWLAN applications," *Microw. Opt. Technol. Lett.*, Vol. 49, No. 1, 97–100, Nov. 2006.

15. Taflove, A. and S. C. Hagness, *Computational Electrodynamics: The Finite Difference Time Domain Method*, 3rd Edition, Artech House, Norwood, MA, 2005.
16. Gedney, S. D., "An anisotropic perfectly matched layer-absorbing medium for the truncation of FDTD lattices," *IEEE Trans. Antennas Propagat.*, Vol. 44, No. 12, 1630–1639, Dec. 1996.
17. Chahat, N., M. Zhadobov, R. Augustine, and R. Sauleau, "Human skin permittivity models for millimetre-wave range," *Electron. Lett.*, Vol. 47, No. 7, 427–428, 2011.
18. Yaghjian, A. D., "Improved formulas for the Q of antennas with highly lossy dispersive materials," *IEEE Antennas Wireless Propag. Lett.*, Vol. 5, 365–369, 2006.
19. Chu, L. J., "Physical limitations of omni-directional antennas," *J. Appl. Phys.*, Vol. 19, 1163–1175, Dec. 1948.
20. Stutzman, W. L. and G. A. Thiele, *Antenna Theory and Design*, 2nd Edition, Wiley, New York, 1997.
21. Caratelli, D. and A. Yarovoy, "Unified time- and frequency-domain approach for accurate modeling of electromagnetic radiation processes in ultra-wideband antennas," *IEEE Trans. Antennas Propagat.*, Vol. 58, No. 10, 3239–3255, Oct. 2010.
22. Romano, N., G. Prisco, and F. Soldovieri, "Design of a reconfigurable antenna for ground penetrating radar applications," *Progress In Electromagnetics Research*, Vol. 94, 1–18, 2009.
23. Caratelli, D., L. P. Ligthart, and A. Yarovoy, "Design and analysis of antennas for GPR applications," *Tech. Rep. IRCTRS04107*, Delft University of Technology, The Netherlands, Sep. 2007.
24. Caratelli, D. and A. Yarovoy, "Design and full-wave analysis of cavity-backed resistively loaded circular-end bow-tie antennas for GPR applications — Part I," *Appl. Comput. Electrom.*, Vol. 25, No. 10, 809–817, Oct. 2010.
25. Caratelli, D. and A. Yarovoy, "Design and full-wave analysis of cavity-backed resistively loaded circular-end bow-tie antennas for GPR applications — Part II," *Appl. Comput. Electrom.*, Vol. 25, No. 10, 818–829, Oct. 2010.
26. Pramudita, A. A., A. Kurniawan, A. B. Suksmono, and A. A. Lestari, "Effect of antenna dimensions on the antenna footprint in ground penetrating radar applications," *IET Microw. Antennas Propag.*, Vol. 3, No. 8, 1271–1278, 2009.
27. Agilent Technologies, Inc., http://www.agilent.com/.